IEEE Access
Multidisciplinary | Rapid Review | Open Access Journal

Received June 16, 2021, accepted June 30, 2021, date of publication July 5, 2021, date of current version July 13, 2021.

Digital Object Identifier 10.1109/ACCESS.2021.3094526

Analysis of Transmission Loss and Boresight Error of a Curved FSS Radome-Enclosed Antenna

HOKEUN SHIN[1], (Student Member, IEEE), DAEYEONG YOON[1], (Student Member, IEEE), DONG-YEOP NA[2], (Member, IEEE), AND YONG BAE PARK[1,3], (Senior Member, IEEE)

[1]Department of AI Convergence Network, Ajou University, Suwon, Gyeonggi-do 16499, South Korea
[2]School of Electrical and Computer Engineering, Purdue University, West Lafayette, IN 47907, USA
[3]Department of Electrical and Computer Engineering, Ajou University, Suwon, Gyeonggi-do 16499, South Korea

Corresponding author: Yong Bae Park (yong@ajou.ac.kr)

This work was supported in part by the Basic Science Research Program through the National Research Foundation of Korea (NRF) funded by the Ministry of Science and ICT under Grant 2020R1A2B5B01002251, and in part by the National Research Foundation of Korea (NRF) grant funded by the Korea Government (MSIT) under Grant 2021R1A4A1030775.

ABSTRACT In this paper, we numerically study a curved frequency selective surface (FSS) radome, which encloses a waveguide slot array antenna operating at 10GHz, using the ray tracing technique and flat model. The transmission loss (TL) and boresight error (BSE) are calculated for various degrees of freedom, such as elevation and azimuth angular scanning or gimbal systems of array antennas to examine the electromagnetic properties of the curved FSS radome. Our calculations of radiation patterns, TL, and BSE for a multi-layered dielectric radome are compared with those of a commercial EM solver for validation. Importantly, we quantify phase distortions, incurred by the curved FSS radome, using the insertion phase delay (IPD) of transmitted fields on the radome surface. Thereby, we demonstrate that the BSEs strongly depend on (1) the spatial distribution of phase distortions on the radome surface and (2) their average level. The present method is highly suited for analyzing radomes with arbitrary surface patterns inserted.

INDEX TERMS Frequency selective surface (FSS), FSS radome, insertion phase delay (IPD), phase distortion, boresight error (BSE), ray tracing technique.

I. INTRODUCTION

An airborne radome protects an enclosed antenna against adverse external environments, primarily looking streamlined to meet the aerodynamic requirements [1]. But it may significantly alter the original specification of the antenna's radiation: transmission loss (TL) and insertion phase delay (IPD) are caused when electromagnetic (EM) waves passing through the radome wall [1], [2], and phase distortions are incurred by IPDs, leading to boresight error (BSE) along with the asymmetric radome geometry. These may degrade the system performance of airborne radars, such as target detection probability and radar cross section (RCS) [1], [2]. Therefore, rigorous EM analyses of radomes should precede the design of airborne radar systems.

There have been various numerical or experimental works to study the EM properties of radome-enclosed antenna systems. For example, homogenous [3] and inhomogeneous [4] planar and tangent-ogive [5]–[8] and Von Karman [9]–[11] dielectric radomes were investigated. Optimization methods were utilized for enhanced dielectric radomes [12]–[18]. Homogeneous radomes were designed based on local uniform thickness [12] and various thickness radome (VTR) [13]–[16], and their BSEs were optimized by analyzing the incident angle variation characteristics for different radome areas. Furthermore, inhomogeneous media, providing a good impedance match, were used [15]–[18] to improve the BSE performance.

Naïve dielectric radomes usually have greater RCS due to the broadband response to transmission and reflection characteristics. Instead, a curved frequency selective surface (FSS), offering the tunability of the bandpass or bandstop functions over a relatively wider bandwidth, can be inserted into radomes to reduce RCS and obtain the stealth performance. Various configurations of FSS radome-enclosed antennas were examined [19]–[29]. For instance, the transmission characteristics of FSS radomes were analyzed by using pole residue matching [19] and ray tracing technique [20]–[22], a hemispherical reconfigurable FSS radome with water channels was studied [23], and the IPD characteristics of planar

The associate editor coordinating the review of this manuscript and approving it for publication was Giorgio Montisci.

FSS radomes were intensively discussed in [24]–[28]. However, previous studies only focused on analyzing the transmission and IPD properties, not BSEs. Although more recent works evaluated TL and BSE of curved FSS radomes [29], the phase distortion effects on BSE have not been investigated yet.

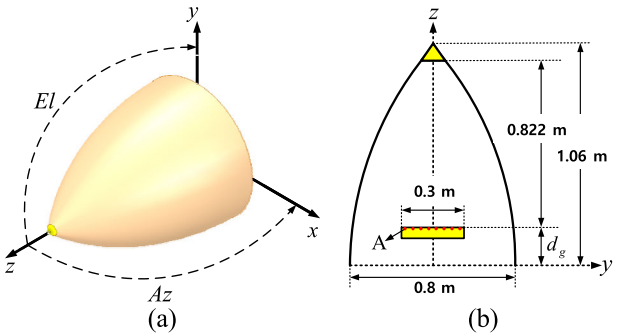

FIGURE 1. Problem geometry. (a) 3-D view. (b) 2-D cross section.

This paper numerically studies the EM characteristics of a curved FSS (hash-shaped slot FSS unit cells) embedded in the tangent-ogive radome, which encloses a waveguide slot array antenna (see Fig. 1). Based on the ray tracing technique and flat model [8], we calculate TL and BSE of the curved FSS radome for various degrees of freedom, including elevation/azimuth angular scanning and gimbal systems of the antenna. Using a commercial EM solver (ANSYS HFSS [30]), we extract the reflection and transmission coefficients and IPD of the FSS layer at a given incident angle for parallel and perpendicular polarizations. Our calculations of radiation patterns, TL, and BSE for a multi-layered dielectric radome are compared with those of a commercial EM solver [31] for validation. Importantly, we quantify phase distortions, incurred by the curved FSS radome, by computing the IPD of transmitted fields on the radome surface. Thereby, we demonstrate that the BSEs strongly depend on (1) the spatial distribution of phase distortions on the radome surface and (2) their average level.

II. ANALYSIS PROCEDURE

A. FAR-FIELD CALCULATION OF FSS RADOME-ENCLOSED ANTENNA SYSTEM

Fig. 1 depicts the problem geometry illustrating a tangent-ogive FSS radome encloses a waveguide slot array antenna. The base diameter and height of the radome are 800 mm and 1060 mm, respectively, and the radome is equipped with a metallic tip, which can be regarded as a perfect electric conductor (PEC) in the microwave regime. Here, we consider the same waveguide slot array antenna (112 radiating elements) used in [8]. The antenna is fixed to a gimbal system to facilitate the scanning purpose, separated from the radome base by $d_g = 200$ mm. Thus, an arbitrary point on the antenna surface should be transformed into the radome coordinate system for an arbitrary gimbal angular rotation. The transformation relates gimbal rotations to the standard two-axis antenna azimuth (Az) and elevation (El) gimbal rotations [1], given by

$$\begin{bmatrix} x \\ y \\ z \end{bmatrix} = \begin{bmatrix} \cos Az & 0 & \sin Az \\ -\sin El \sin Az & \cos El & \sin El \cos Az \\ -\cos El \sin Az & -\sin El & \cos El cos Az \end{bmatrix} \times \begin{bmatrix} x_l \\ y_l \\ z_l \end{bmatrix} + \begin{bmatrix} 0 \\ 0 \\ d_g \end{bmatrix} \quad (1)$$

It is assumed that the gimbal system has no rotational offsets, viz, the El over Az (El/Az) antenna gimbal case. Note that El and Az represent the gimbal rotations in the y−z and x − z planes, respectively (see Fig. 1 (a)). The reference Cartesian coordinate system is at the center of the radome base. We define (x_l, y_l, z_l) and (x_l^n, y_l^n, z_l^n) as the local coordinate system at the center of the antenna surface and the location of the n^{th} radiating slot on the planar array antenna (marked by A in Fig. 1 (b)), respectively, as depicted in Fig. 1 (b).

To evaluate the EM performance of the FSS radome-enclosed antenna system, we use the ray tracing technique and the flat model proposed in [8]. In the high-frequency regime, the curved radome can be looked locally flat based on the tangent plane approximation (it is valid when the wavelength is short since phase matching happens locally, and the law of reflection, transmission, and Snell's law are satisfied approximately.). Note that "flat model" refers to a flat multi-layer radome with the same structure as an original curved radome. This method uses a look-up table including the pre-computed reflection and transmission coefficients of the flat model, significantly reducing costly computational loads of the full-wave analyses with relatively higher accuracy. Therefore, the present method is highly suitable for the EM analysis of a multi-layer radome with an embedded curved FSS layer.

We model radiating elements of the array antenna by point sources located at the center of each slot. Note that the tangential electric field on each slot is supposed to have a y_l-component (E_{y_l}) in the local coordinate system. The equivalent magnetic currents, obtained from the use of surface equivalence theorem [32], generate the rays propagating toward the FSS radome wall. Then, the intersection points of the rays and the radome surface are determined, and the reflected and transmitted waves are calculated. If the intersection point is placed on the metal tip, there are only reflected waves phase reversed; otherwise, the reflected and transmitted waves are calculated using the pre-computed reflection and transmission coefficients of the flat model. The reflected wave is traced using the ray tracing technique until the transmitted wave reaches the outermost radome surface. Finally, the Huygens's principle is applied to the EM fields on the outermost radome surface to obtain equivalent electric and magnetic surface currents that produce the radiated fields in the far-field regions.

B. PHASE DISTORTION COMPUATION OF FLAT MODEL AND CURVED RADOME

The transmission coefficients of the perpendicular and parallel polarizations of the flat model are complex-valued (magnitude and phase angle). The phase angle includes a phase shift introduced by the insertion of the radome wall into the propagation path. Such phase shift is known as the IPD, which can be obtained by compensating the free space phase shift from the phase angle of the transmission coefficient [33] in the presence of the FSS radome, given by

$$IPD_{\perp/\parallel} = \angle T_{\perp/\parallel} - \frac{2\pi}{\lambda_0} t \cos\theta_i \tag{2}$$

where t is the thickness of the radome wall and θ_i is the incident angle. Note that $\perp$ and $\parallel$ denote the perpendicular and parallel polarizations, respectively. The phase distortion, which represents the degree of distortions in the transmitted wavefront, is caused by IPD, leading to BSE. We first analyze the effects of the phase distortion of the flat model on the BSE. Since the EM refraction does not occur at the normal incidence to the radome wall, the phase distortion for a given incident angle θ_i can be defined by [3]

$$\psi^d_{\perp/\parallel} = IPD^{\theta_i}_{\perp/\parallel} - IPD^{0^\circ}_{\perp/\parallel} \tag{3}$$

where $\psi^d_\perp$ and $\psi^d_\parallel$ are the phase distortions of perpendicular and parallel polarizations of the flat model, respectively. In general, the phase distortion gets larger with the increase of the incident angle, and the BSE is directly proportional to the largest phase distortion. Since above $\psi^d_\perp$ and $\psi^d_\parallel$ are of the flat model, we should take into account the radome curvature shape to evaluate the actual phase distortion effects on the BSE. It can be calculated from the phase of transmitted electric fields. At an arbitrary point on the radome surface, the transmitted electric field can be expressed by

$$\vec{E}^t = \sum_{n=1}^{N} \vec{E}^i_{n,\perp} T_{n,\perp} + \vec{E}^i_{n,\parallel} T_{n,\parallel} \tag{4}$$

where $\vec{E}^i_{n,\perp}$ and $\vec{E}^i_{n,\parallel}$ are the perpendicular and parallel components of electric fields radiated from a n^{th} slot antenna, respectively, and $T_{n,\perp}$ and $T_{n,\parallel}$ are transmission coefficients of the perpendicular and parallel polarizations, respectively. Rewriting (3) in the Cartesian coordinate system by

$$\vec{E}^t = E^t_x e^{j\phi^t_x}\hat{a}_x + E^t_y e^{j\phi^t_y}\hat{a}_y + E^t_z e^{j\phi^t_z}\hat{a}_z \tag{5}$$

where the phase terms of the transmitted electric field can be transformed via (1), one can derive

$$IPD_{r,c} = \phi^t_c - \phi^0_c \tag{6}$$

where $IPD_{r,c}$ ($c = x, y,$ *and* z) is the IPD of the curved radome and ϕ^0_c is the phase of transmitted electric fields in the absence of the radome (i.e., free space). Similar to (2), the phase distortion of the curved radome can be calculated via

$$\psi^d_{r,c} = IPD_{r,c} - IPD^{0^\circ}_{\perp or \parallel} \tag{7}$$

In the following section, we study the relation between $\psi^d_{r,c}$ ($c = x, y,$ *and* z) and BSE observing its spatial distribution over the curved radome surface and average level for the El and Az scanning.

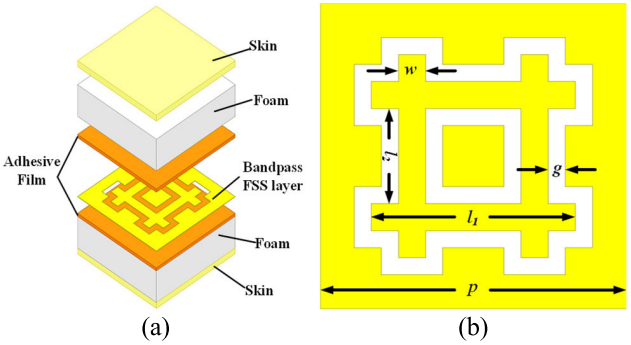

FIGURE 2. Geometry of the FSS radome structure. (a) Perspective view. (b) Hash-shaped slot FSS unit cell.

III. NUMERICAL RESULTS

A. EM CHARACTERISTICS OF FSS RADOME

The tangent ogive FSS radome was analyzed around the center frequency of 10 GHz. We utilized the conventional hash-shape, one of the well-known FSS unit cell patterns, following the typical design procedure [33], [34]. As illustrated in Fig. 2, the FSS radome consists of seven layers: the innermost and outermost layers are E-glass/epoxy (skin), second and sixth layers are foam, third and fourth layers are adhesive films, and a FSS layer (hash-shaped slot unit cells) is sandwiched by the films. The dielectric properties for all layers and design parameters are given in Table 1 and 2, respectively. We also consider the dielectric radome without the FSS layer for validation and performance comparison.

TABLE 1. Dielectric properties of FSS radome.

Material	ε_r	tanδ	Thickness
E-glass/epoxy	4.348	0.013	0.84 mm
Adhesive Film	3.003	0.019	0.12 mm
Foam	1.103	0.0038	3.00 mm
FSS layer (copper)	-	-	0.02 mm

TABLE 2. Design parameters of FSS unit cell with hash-shaped slot.

Parameters	Length	Parameters	Length
p	4.5 mm	w	0.2 mm
g	0.1 mm	l_1	4.0 mm
l_2	1.3 mm	-	-

Before studying the TL and the BSE of the curved FSS radome, we first study the reflection and transmission behaviors of the FSS flat model. We extract the reflection and transmission coefficients at a given incident angle for both

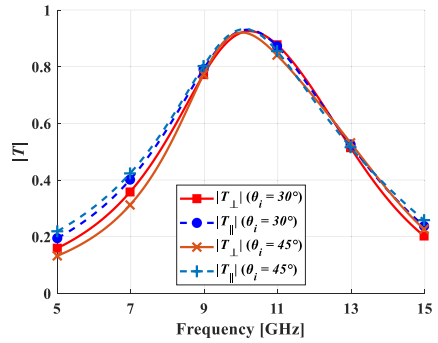

FIGURE 3. Transmission characteristic of the FSS flat model.

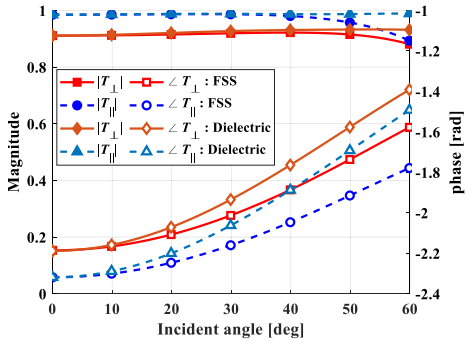

FIGURE 4. Transmission coefficients of the FSS and dielectric flat models.

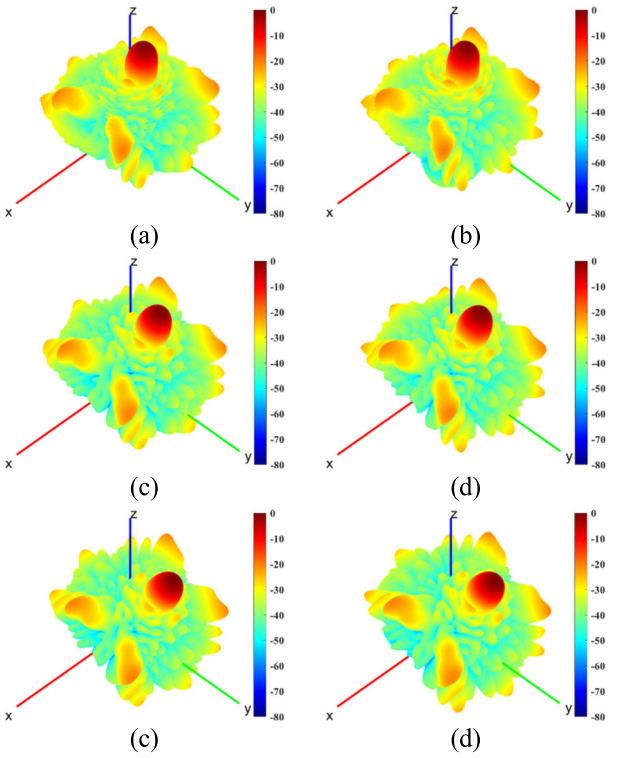

FIGURE 5. Three dimensional normalized radiation patterns of the dielectric radome-enclosed antenna system for El scanning. (a) our method at 10°. (b) MWS of CST at 10°. (c) our method at 20°. (d) MWS of CST at 20°. (e) our method at 30°. (f) MWS of CST at 30°.

polarizations using the ANSYS HFSS. As the maximum incident angle for the employed radome was 57.6°, the simulation was conducted the scanning over the incident angle range [0°, 60°]. Fig. 3 shows the transmission characteristics of the FSS flat model versus frequency. The FSS flat model has a passband characteristic in the X-band. Figs. 4 illustrates the transmission coefficients of the FSS and dielectric flat models. The transmission coefficients of the FSS flat model, ranging from 0.88 to 0.93, are smaller than those of the dielectric flat model due to the higher loss of the FSS layer. This is because of the ohmic loss in addition to the dielectric loss. More specifically, the FSS layer can be represented by a shunt complex admittance in the equivalent transmission line model; hence, the ohmic loss occurs owing to the real part of the admittance [33], [34]. Moreover, the transmission coefficients of the perpendicular polarization for both cases rapidly decrease in the incident angle range [40°, 60°], whereas those of the parallel polarization do not change significantly. This can increase the TL at gimbal angles including the incident angle range [40°, 60°] due to the transmission coefficients of the perpendicular polarization.

Before analyzing the FSS radome, we consider the dielectric radome without the FSS layer to validate our method. Figs 5 and 6 show three dimensional radiation patterns calculated by our method and microwave studio (MWS) of CST [31] at the gimbal angles of 10°, 20°, and 30° for the El and Az scanning, respectively. There is an excellent agreement in the results of two methods. In addition, we compared normalized radiation pattern, TL, and BSE of the dielectric

TABLE 3. TL and BSE of the multi-layer dielectric radome.

Gimbal angle		Our method		MWS of CST	
		TL [dB]	BSE [mrad]	TL [dB]	BSE [mrad]
	0°	0.53	0	0.63	0
	10°	0.54	-0.70	0.64	-0.78
El	20°	0.21	-0.52	0.22	-0.35
	30°	0.16	0.17	0.18	0.17
	10°	0.19	5.24	0.16	6.10
Az	20°	0.10	0.52	0.06	0.44
	30°	0.12	1.05	0.10	1.13

radome with those of MWS of CST in Fig. 7, Table 3, respectively. There is an excellent agreement between the results obtained by two methods.

Now, we consider the FSS radome. Note that we assumed that the gimbal angle range was in [0°, 60°] for the El and Az scanning. The TL and the BSE of the FSS radome were calculated by using the reflection and the transmission characteristics of the flat model in Fig. 4. The TL of the FSS radome is shown in Fig. 8, compared with those of the dielectric radome. Since the FSS and dielectric radomes are equipped with a metal tip, they have quite larger TLs at smaller gimbal angles (toward the direction of the metallic tip). In addition, as the transmission coefficients of the perpendicular polarization at higher incident angles are relatively lower than those of lower incident angles, the TL increases at the smaller gimbal angles. The TL of the two radomes

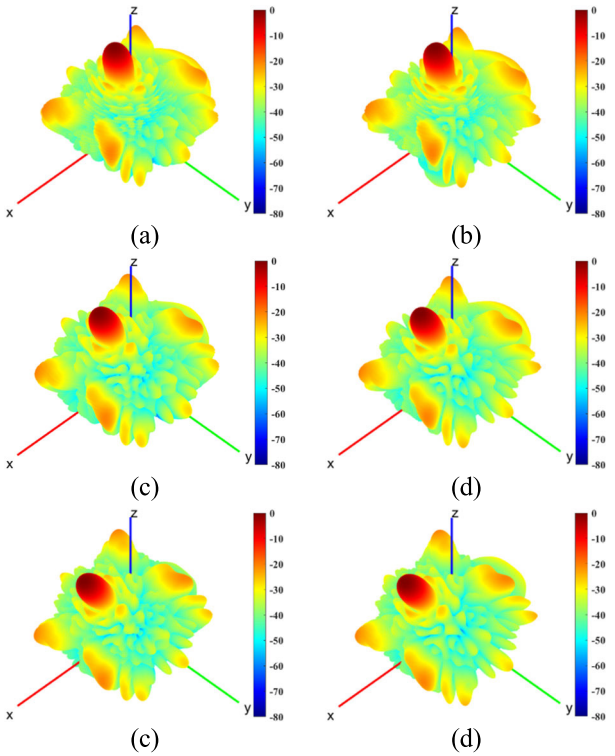

FIGURE 6. Three dimensional normalized radiation patterns of the dielectric radome-enclosed antenna system for Az scanning. (a) our method at 10°. (b) MWS of CST at 10°. (c) our method at 20°. (d) MWS of CST at 20°. (e) our method at 30°. (f) MWS of CST at 30°.

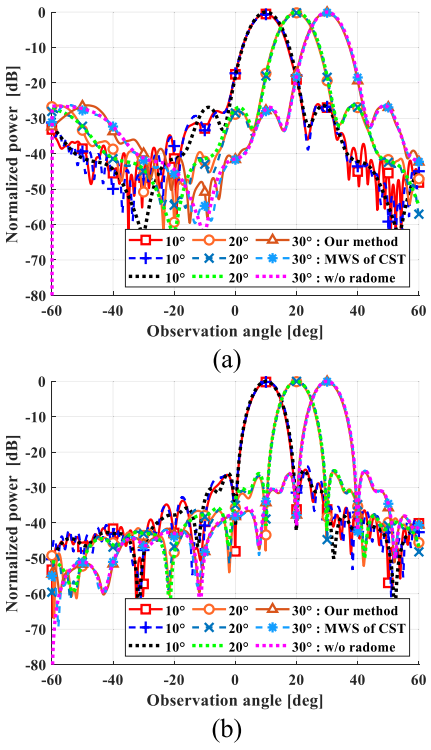

FIGURE 7. Normalized radiation patterns of the dielectric radome-enclosed antenna system. (a) El scanning. (b) Az scanning.

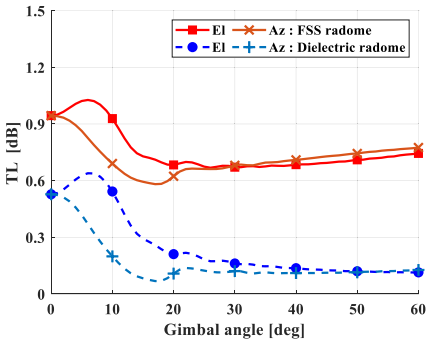

FIGURE 8. TL of the FSS and dielectric radomes for El and Az scanning.

also depends on the gimbal angle and direction. It can be observed in both radomes that, in the gimbal angle range [0°, 20°], TLs for the El scanning are smaller than those for the Az scanning, and they are getting closer gradually with the increase of the gimbal angle. In addition, the TL of the FSS radome is smaller than those of the dielectric radome. From these results, we can deduce that the TL has a similar tendency with the transmission coefficients at incident angles corresponding to each gimbal angle.

Fig. 9 shows the BSE of the FSS and dielectric radomes. The BSE also depends on the gimbal angle and direction. For the El scanning, the two radomes have relatively large BSE at the gimbal angle range [0°, 20°], where the BSE of the FSS radome is smaller than that of the dielectric radome. With the increase of the gimbal angles, BSEs for both cases quickly decrease, converging to 0 mrad with small fluctuations. The FSS and dielectric radomes have the maximum BSE at the gimbal angle of 5°, which are -5.585 and -6.807 mrad, respectively. For the Az scanning, The BSE of the FSS radome is smaller than that of the dielectric radome. The two radomes have very large BSE at the gimbal angles of 0° to 20°, while having very small BSE at gimbal angles greater than about 20°. The maximum BSE of the FSS and dielectric radomes is 4.014 and 5.411 mrad at the gimbal angle of 11°, respectively. We confirmed that the TL of the FSS radome was larger than that of the dielectric radome due to the loss of the FSS layer, whereas its BSE was generally smaller.

B. PHASE DISTORTION AND BORESIGHT ERROR

Radome area illuminated by the radiated beam of the antenna directly affects the EM performance of curved radomes. Thus, we study the average power density on the radome surface. Fig. 10 depicts distributions of the average power density within the radome surface projected by the antenna aperture at the El gimbal angles of 0°, 10°, 20°, and 30°. To facilitate the comparison of them for the scanning, the local coordinate system defined in Section II.A was used. Since the EM wave cannot be transmitted through the metal tip, the metal tip part is not plotted (see Figs. 10 (a) and (b)). It is clearly observed that the hot spots of the average power density are distributed within a radius of about 0.1 m in all cases. Although other cases for the Az scanning are not shown in this paper, they also have similar results. It implies that the

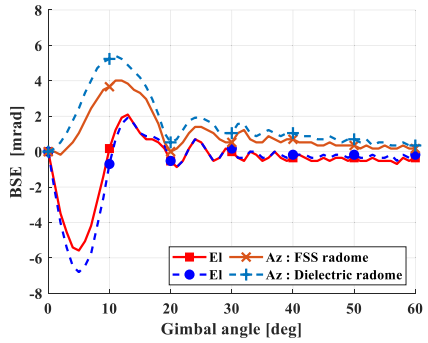

FIGURE 9. BSE of the FSS and dielectric radomes for El and Az scanning.

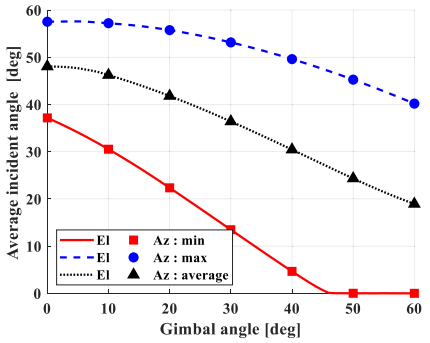

FIGURE 11. Maximum, minimum, and average incident angles in radome area.

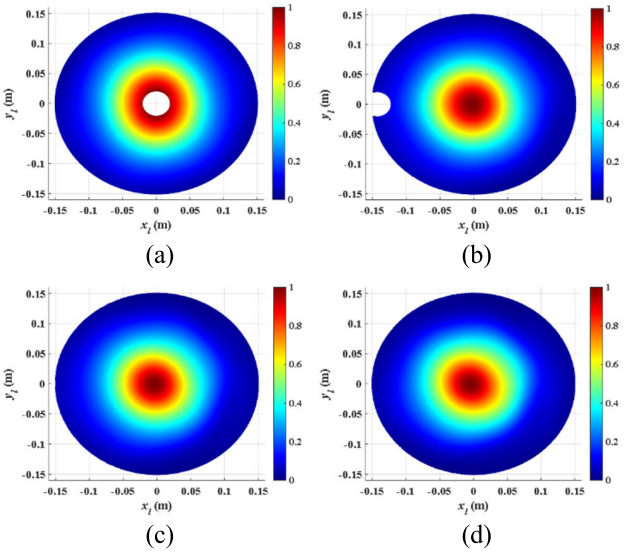

FIGURE 10. Average power density distribution for El scanning. (a) 0°. (b) 10°. (c) 20°. (d) 30°.

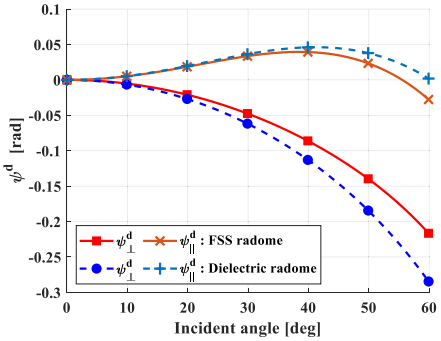

FIGURE 12. $\psi_{\perp}^{d}$ and $\psi_{\parallel}^{d}$ of the FSS and dielectric flat models.

radome area within the radius of 0.1 m mainly contributes to the EM performance of the curved radome; hence, we only consider the radome area within the radius of 0.1 m to evaluate the EM performance of the curved radome in the following numerical calculations. Fig. 11 illustrates the minimum, maximum, and average incident angles in the radome area for the El and Az scanning. The incident angles for the El and Az scanning are the same, but the EM characteristics of the FSS and dielectric radomes are different depending on the scanning direction. This means that even if the gimbal angle is the same, the impact of the perpendicular and parallel polarizations at the intersection point on the surface of the radome depends on the scanning direction.

Fig. 12 shows the phase distortion of the FSS and dielectric flat models, which implying that the phase distortion strongly depends on the polarization and the incident angle. For the FSS and dielectric models, the phase distortions of the perpendicular polarization are positive, whereas those of the parallel polarization are negative. In addition, the magnitude of the phase distortions of the perpendicular polarization is relatively smaller than that of the parallel polarization. Note that the phase distortions of the FSS model are smaller than those of the dielectric model. As mentioned in Section III.A, the FSS acts as a shunt admittance in the equivalent transmission line model of the flat model, which can reduce the phase distortion in combination with the series inductance representing the dielectrics in the equivalent transmission line model [33], [34]. Since the BSE tends to be proportional to the magnitude of the phase distortion in the incident angle range, the BSE of the FSS radome decreases. This is why the BSE of the FSS radome is generally smaller than that of the dielectric radome in Fig. 4. From these results, we confirmed the effects of the phase distortion of the flat model on the BSE. However, even if the phase distortion is not 0 rad, it seems insufficient to explain the relation between the phase distortion and the BSE when the BSE is close to 0 mrad.

In order to analyze the relation between the $\psi_{r,c}^{d}$ ($c = x, y,$ *and* z) and the BSE, the $\psi_{r,c}^{d}$ distributions on the radome area were analyzed for the El and Az scanning. The $\psi_{r,c}^{d}$ distributions are plotted using the local coordinate system, as shown in the results in Fig. 10. As the tangential electric field on each slot of the enclosed antenna has only the y_l-component, the transmitted electric field $\vec{E}^{t}$ has a dominant component $E_{y_l}^{t}$. Thus, we assumed that only the $E_{y_l}^{t}$ affected the BSE and considered the $\psi_{r,y}^{d}$ in the evaluation. Here the $\psi_{r,y}^{d}$ distributions of the FSS and dielectric radomes were calculated at some gimbal angles as examples to investigate

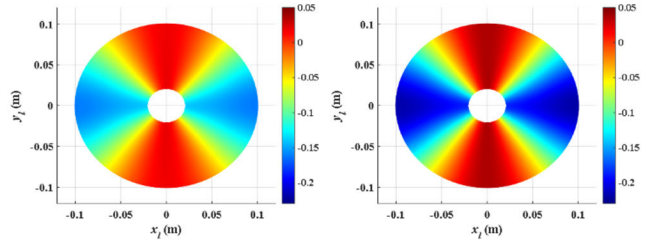

FIGURE 13. $\psi_{r,y}^{d}$ distribution at gimbal angle of 0°. (a) FSS radome. (b) dielectric radome.

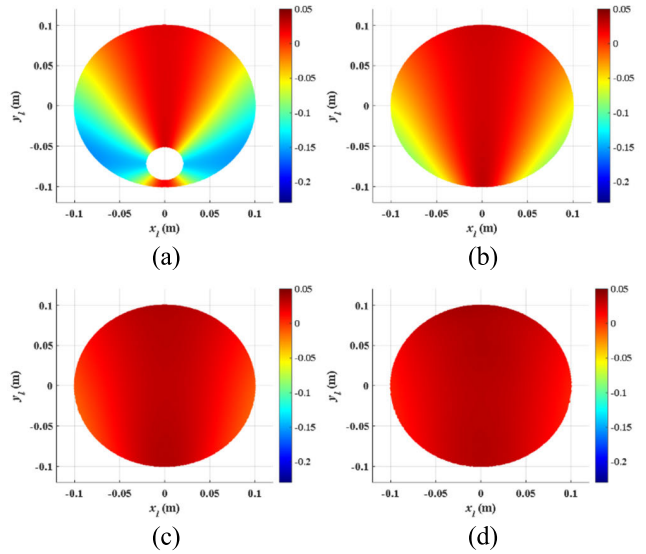

FIGURE 14. $\psi_{r,y}^{d}$ distribution of the FSS radome for El scanning. (a) 5°. (b) 10°. (c) 20°. (d) 30°.

their variation characteristics. All examples are plotted in the same range in order to facilitate the comparison of them. The $\psi_{r,y}^{d}$ distributions of the FSS and dielectric radomes at a gimbal angle of 0° are shown in Fig. 13. In addition, at the El and Az gimbal angles of 5°, 10°, 20°, and 30°, the $\psi_{r,y}^{d}$ distributions of the FSS and dielectric radomes are plotted in Figs. 14, 15, 16, and 17, respectively. It is seen that the two radomes have a similar distribution, but the FSS radome have a smaller magnitude of the $\psi_{r,y}^{d}$ than the dielectric radome. At the gimbal angle of 0°, the $\psi_{r,y}^{d}$ of the FSS and dielectric radomes is distributed as two hourglass shapes based on the x_l- (corresponding to blue color) and y_l- axes (corresponding to red color), respectively. The perpendicular polarization is a dominant component in the hourglass shape based on x_l-axis, whereas the parallel polarization is a dominant component in the hourglass shape based on y_l-axis. In addition, the $\psi_{r,y}^{d}$ distributions of the two radomes are rotationally symmetric. The BSE tends to increase with the increase of the phase distortion, but the BSE of the two radomes is 0 mrad. This is because the $\psi_{r,y}^{d}$ distributions of the two radomes are rotationally symmetric. In other words, the BSE is immune to the $\psi_{r,y}^{d}$ in the rotationally symmetric $\psi_{r,y}^{d}$ distribution,

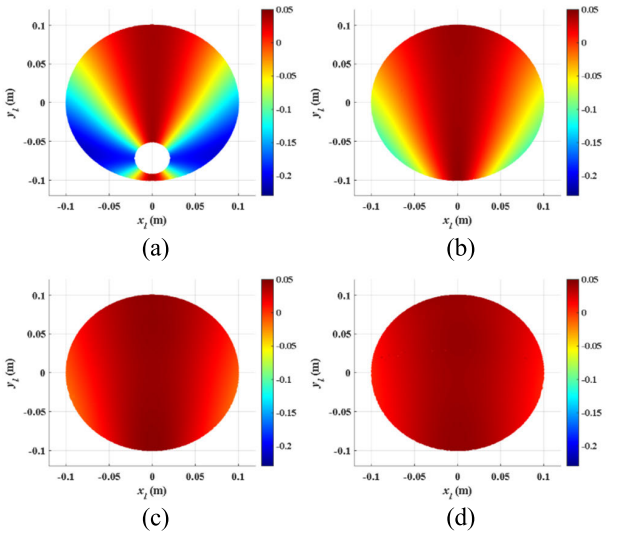

FIGURE 15. $\psi_{r,y}^{d}$ distribution of the dielectric radome for El scanning. (a) 5°. (b) 10°. (c) 20°. (d) 30°.

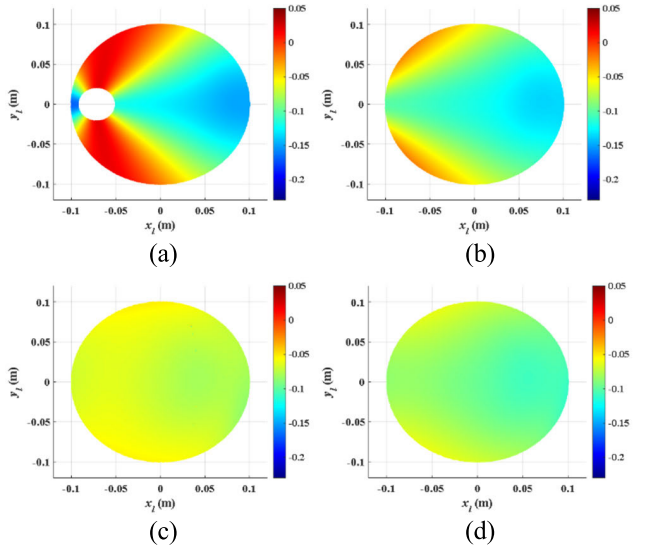

FIGURE 16. $\psi_{r,y}^{d}$ distribution of the FSS radome for Az scanning. (a) 5°. (b) 10°. (c) 20°. (d) 30°.

and it is always 0 mrad. In Figs. 14, 15, 16, and 17, the $\psi_{r,y}^{d}$ distributions of the two radomes show the following characteristics.

1) For the El scanning, the area mainly affected by the parallel polarization gradually increases, whereas the area mainly affected by the perpendicular polarization gradually increases for the Az scanning.
2) At the El and Az gimbal angles of 5° and 10°, the $\psi_{r,y}^{d}$ distributions of the two radomes have non-uniform values corresponding to blue, yellow, red, etc., and are asymmetrical.
3) At the El and Az gimbal angles of 20° and 30°, the $\psi_{r,y}^{d}$ distributions have a nearly constant value corresponding to either red color or yellow-green color depending

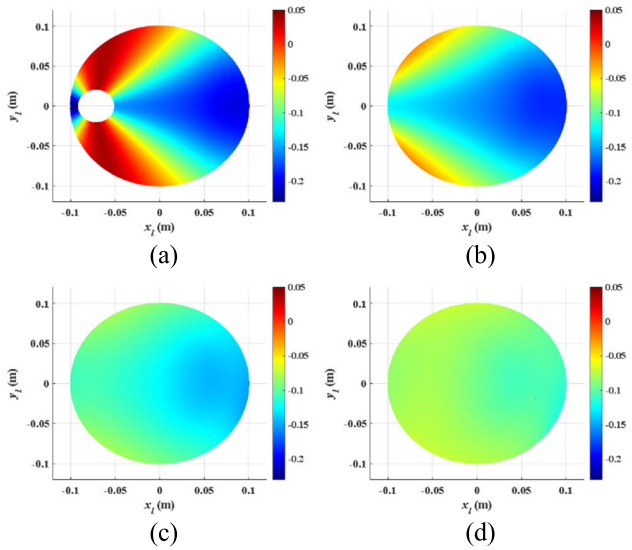

FIGURE 17. $\psi^d_{r,y}$ distribution of the dielectric radome for Az scanning. (a) 5°. (b) 10°. (c) 20°. (d) 30°.

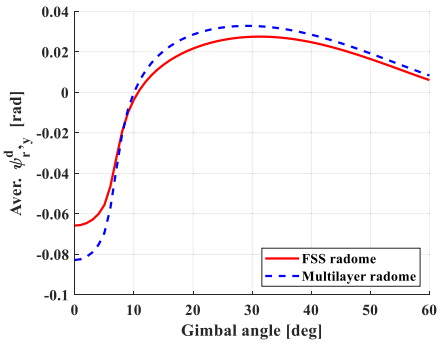

FIGURE 18. Average of $\psi^d_{r,y}$ distribution for El scanning.

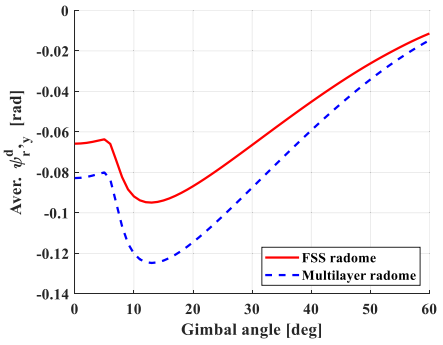

FIGURE 19. Average of $\psi^d_{r,y}$ distribution for Az scanning.

on the gimbal direction. Thus, it seems to be close to the rotationally symmetry.

Figs. 18 and 19 show the average of the $\psi^d_{r,y}$ distributions of the FSS and dielectric radomes for the El and Az scanning, respectively. It seems that the BSE is proportional to the average of the $\psi^d_{r,y}$ distribution at the El and Az gimbal angles of 5° and 10°. In particular, note the BSE of the two radomes,

TABLE 4. Summary of BSE and $\psi^d_{r,y}$ for El scanning.

El gimbal angle		5°	10°	20°	30°
FSS radome	BSE [mrad]	-5.6	0.2	-0.5	0
	Aver. $\psi^d_{r,y}$ [rad]	-0.056	-0.004	0.022	0.027
	Symmetry (√) or asymmetry (x)	x	x	√	√
Dielectric radome	BSE [mrad]	-6.8	-0.7	-0.5	0.2
	Aver. $\psi^d_{r,y}$ [rad]	-0.07	0	0.029	0.033
	Symmetry (√) or asymmetry (x)	x	x	√	√

TABLE 5. Summary of BSE and $\psi^d_{r,y}$ for Az scanning.

Az gimbal angle		5°	10°	20°	30°
FSS radome	BSE [mrad]	1	3.7	0	0.5
	Aver. $\psi^d_{r,y}$ [rad]	-0.064	-0.092	-0.087	-0.066
	Symmetry (√) or asymmetry (x)	x	x	√	√
Dielectric radome	BSE [mrad]	2.4	5.2	0.5	1
	Aver. $\psi^d_{r,y}$ [rad]	-0.08	-0.12	-0.115	-0.088
	Symmetry (√) or asymmetry (x)	x	x	√	√

0.2 and -0.7 mrad respectively, at the El gimbal angle of 10°. Although their $\psi^d_{r,y}$ distributions are asymmetric, their BSE is very small due to the lower average of their $\psi^d_{r,y}$ distributions, -0.004 and 0 rad, respectively. On the other hand, at the El and Az gimbal angle of 20° and 30°, the BSE is close to 0 mrad irrespective of the average of the $\psi^d_{r,y}$ distribution. Table 4 and 5 summarize the aforementioned results. From these results, we can find the relation between the BSE and the phase distortion of the curved radome. The BSE is determined by the combination of the $\psi^d_{r,y}$ distribution and its average and has the two characteristics as follows.

1) For the rotationally symmetric $\psi^d_{r,y}$ distribution, the BSE is very small (close to 0 mrad) regardless of its average.
2) For the asymmetric $\psi^d_{r,y}$ distribution, the BSE is proportional to its average.

We confirmed that the effects of the phase distortions of the flat model and curved radome on the BSE. The maximum BSE increased with the increase of the phase distortion of the flat model. The $\psi^d_{r,y}$ causes the BSE in combination with the radome asymmetry. These results can be used to analyze the FSS radome and improve its EM performance.

IV. CONCLUSION

We have calculated the TL and the BSE of tangent-ogive FSS radome using the ray tracing technique and the flat model. In addition, we have analyzed the phase distortions of the flat model and curved radome to investigate their effects on the BSE. Our method has been validated comparing the computation results with those of the commercial EM simulator.

The TL of the FSS radome was larger than those of the dielectric radome, whereas the its BSE was generally smaller. We have confirmed that the BSE of the FSS radome were smaller than those of the dielectric radome because the phase distortion of the FSS flat model were smaller than those of the dielectric flat model in the incident angle range. Moreover, we have found that the BSE depended on the two characteristics of the phase distortion of the curved radome: the phase distortion distribution and its average. For the rotationally symmetrical phase distortion distribution, the BSE was very small (close to 0) irrespective of the average of the phase distortion distribution. On the other hand, for the asymmetrical phase distortion distribution, the BSE increased with the average of the phase distortion distribution. Our method is useful to analyze FSS radomes, and these results can be used to improve the EM performance of FSS radomes such as the BSE correction.

REFERENCES

[1] D. J. Kozakoff, *Analysis of Radome-Enclosed Antennas*, 2nd ed. Norwood, MA, USA: Artech House, 2010.

[2] G. A. E. Crone, A. W. Rudge, and G. N. Taylor, "Design and performance of airborne radomes: A review," *IEE Proc. F Commun., Radar Signal Process.*, vol. 128, no. 7, pp. 451–464, Dec. 1981.

[3] P. J. Carroll and J. R. Chesnut, "Ka-band radome design," Dept. Aero-Electron. Technol., Naval Air Develop. Center, Warminster, PA, USA, Tech. Rep. NADC-AE-6587, May 1969.

[4] R. U. Nair, S. Shashidhara, and R. M. Jha, "Novel inhomogeneous planar layer radome design for airborne applications," *IEEE Antennas Wireless Propag. Lett.*, vol. 11, pp. 854–856, Jul. 2012.

[5] D. Burks, E. Graf, and M. Fahey, "A high-frequency analysis of radome-induced radar pointing error," *IEEE Trans. Antennas Propag.*, vol. AP-30, no. 5, pp. 947–955, Sep. 1982.

[6] R. Orta, R. Tascone, and R. Zich, "Performance degradation of dielectric radome covered antennas," *IEEE Trans. Antennas Propag.*, vol. 36, no. 12, pp. 1707–1713, Dec. 1988.

[7] K. Siwiak, T. Dowling, and L. Lewis, "Boresight errors induced by missile radomes," *IEEE Trans. Antennas Propag.*, vol. AP-27, no. 6, pp. 832–841, Nov. 1979.

[8] H. Shin, D. Yoon, K. Choi, I. Jung, and Y. B. Park, "Analysis of a curved multi-layer radome using a flat model and the ray tracing technique," *J. Electr. Eng. Technol.*, vol. 15, no. 2, pp. 787–794, Mar. 2020.

[9] P. L. Overfelt, "Superspheroids: A new family of radome shapes," *IEEE Trans. Antennas Propag.*, vol. 43, no. 2, pp. 215–220, Feb. 1995.

[10] H.-S. Lee and H. Park, "Prediction of radome bore-sight errors using a projected image of source distributions," *Prog. Electromagn. Res.*, vol. 92, pp. 181–194, Jan. 2009.

[11] J. Kim, S. C. Song, H. Shin, and Y. B. Park, "Radiation from a millimeter-wave rectangular waveguide slot array antenna enclosed by a Von Karman radome," *J. Electromagn. Eng. Sci.*, vol. 18, no. 3, pp. 154–159, Jul. 2018.

[12] H. Meng and W. Dou, "Multi-objective optimization of radome performance with the structure of local uniform thickness," *IEICE Electron. Exp.*, vol. 5, no. 20, pp. 882–887, 2008.

[13] R. U. Nair and R. M. Jha, "Electromagnetic performance analysis of a novel monolithic radome for airborne applications," *IEEE Trans. Antennas Propag.*, vol. 57, no. 11, pp. 3664–3668, Nov. 2009.

[14] W. Xu, B. Y. Duan, P. Li, and Y. Qiu, "A new efficient thickness profile design method for streamlined airborne radomes," *IEEE Trans. Antennas Propag.*, vol. 65, no. 11, pp. 6190–6195, Nov. 2017.

[15] W. Xu, P. Li, and Y. Qiu, "Efficient variable thickness radome design with insertion phase delay correction," *Int. J. Antennas Propag.*, vol. 2019, pp. 1–12, Nov. 2019.

[16] W. Xu, B. Y. Duan, P. Li, and Y. Qiu, "Study on the electromagnetic performance of inhomogeneous radomes for airborne applications—Part I: Characteristics of phase distortion and boresight error," *IEEE Trans. Antennas Propag.*, vol. 65, no. 6, pp. 3162–3174, Jun. 2017.

[17] W. Xu, B. Y. Duan, P. Li, and Y. Qiu, "Study on the electromagnetic performance of inhomogeneous radomes for airborne applications—Part II: The overall comparison with variable thickness radomes," *IEEE Trans. Antennas Propag.*, vol. 65, no. 6, pp. 3175–3183, Jun. 2017.

[18] P. S. M. Yazeen, C. V. Vinisha, S. Vandana, M. Suprava, and R. U. Nair, "Electromagnetic performance analysis of graded dielectric inhomogeneous streamlined airborne radome," *IEEE Trans. Antennas Propag.*, vol. 65, no. 5, pp. 2718–2723, May 2017.

[19] E. Martini, F. Caminita, M. Nannetti, and S. Maci, "Fast analysis of FSS radome for antenna RCS reduction," in *Proc. IEEE Antennas Propag. Soc. Int. Symp.*, Jul. 2006, pp. 1801–1804.

[20] U. d'Elia, G. Pelosi, C. Pichot, S. Selleri, and M. Zoppi, "A physical optics approach to the analysis of large frequency selective radomes," *Prog. Electromagn. Res.*, vol. 138, pp. 537–553, Jan. 2013.

[21] J. H. Kim, H. J. Chun, I. P. Hong, Y. J. Kim, and Y. B. Park, "Analysis of FSS radomes based on physical optics method and ray tracing technique," *IEEE Antennas Wireless Propag. Lett.*, vol. 13, pp. 868–871, May 2014.

[22] J. H. Kim, S. Lee, H. Shin, K.-Y. Jung, H. Choo, and Y. B. Park, "Radiation from a cavity-backed circular aperture array antenna enclosed by an FSS radome," *Appl. Sci.*, vol. 8, no. 12, pp. 2346–2354, Nov. 2018.

[23] D.-C. Son, H. Shin, Y. J. Kim, I. P. Hong, H. J. Chun, K.-Y. Jung, H. Choo, and Y. B. Park, "Design of a hemispherical reconfigurable frequency selective surface using water channels," *IEEE Access*, vol. 6, pp. 61445–61451, Oct. 2018.

[24] R. U. Nair, A. Neelam, and R. M. Jha, "A novel jerusalem cross FSS embedded A-sandwich radome for aerospace applications," in *Proc. Appl. Electromagn. Conf. (AEMC)*, Kolkata, India, Dec. 2009, pp. 1–4.

[25] R. U. Nair, J. Madhumitha, and R. M. Jha, "Broadband EM performance characteristics of single square loop FSS embedded monolithic radome," *Int. J. Antennas Propag.*, vol. 2013, pp. 1–8, Mar. 2013.

[26] R. U. Nair and R. M. Jha, "Broadbanding of A-sandwich radome using Jerusalem cross frequency selective surface," *CMC-Comput., Mater. Continua*, vol. 37, no. 2, pp. 109–121, 2013.

[27] S. Narayan, J. B. Shamala, R. U. Nair, and R. M. Jha, "Electromagnetic performance analysis of novel multi-band metamaterial FSS for millimeter wave radome applications," *Comput. Mater. Continua*, vol. 31, no. 1, pp. 1–16, Sep. 2012.

[28] R. U. Nair, A. Neelam, and R. M. Jha, "EM performance analysis of double square loop FSS embedded C-sandwich radome," in *Proc. Appl. Electromagn. Conf. (AEMC)*, Kolkata, India, Dec. 2009, pp. 1–3.

[29] S. Narayan, G. Gulati, B. Sangeetha, and R. U. Nair, "Novel metamaterial-element-based FSS for airborne radome applications," *IEEE Trans. Antennas Propag.*, vol. 66, no. 9, pp. 4695–4707, Sep. 2018.

[30] (2019). *Ansys HFSS*. [Online]. Available: http://www.ansys.com/

[31] (2021). *CST Microwave Studio*. [Online]. Available: https://www.cst.com/

[32] C. A. Balanis, *Advanced Engineering Electromagnetics*, 2nd ed. New York, NY, USA: Wiley, 2012.

[33] J. L. Volakis, *Antenna Engineering Handbook*. New York, NY, USA: McGraw-Hill, 2007.

[34] B. A. Munk, *Frequency Selective Surfaces: Theory and Design*. New York, NY, USA: Wiley, 2005.

HOKEUN SHIN (Student Member, IEEE) received the B.S. degree in electrical and computer engineering from Ajou University, Suwon, South Korea, in 2015, where he is currently pursuing the integrated M.S./Ph.D. degree in AI convergence network. His research interests include frequency selective surface, radomes, and radar cross section.

DAEYEONG YOON (Student Member, IEEE) received the B.S. degree in electrical and computer engineering from Ajou University, Suwon, South Korea, in 2018, where he is currently pursuing the integrated M.S./Ph.D. degree in AI convergence network. His research interests include frequency selective surface, radomes, and radar cross section.

DONG-YEOP NA (Member, IEEE) received the B.S. and M.S. degrees in electrical and computer engineering from Ajou University, Suwon, South Korea, in 2012 and 2014, respectively, and the Ph.D. degree in electrical and computer engineering from The Ohio State University, Columbus, OH, USA, in 2018. He is currently a Research Scientist at Purdue University. His research interests include computational electromagnetics, particle-in-cell, and quantum electromagnetics.

YONG BAE PARK (Senior Member, IEEE) received the B.S., M.S., and Ph.D. degrees in electrical engineering from the Korea Advanced Institute of Science and Technology, South Korea, in 1998, 2000, and 2003, respectively. From 2003 to 2006, he was with the Korea Telecom Laboratory, Seoul, South Korea. He joined the School of Electrical and Computer Engineering, Ajou University, South Korea, in 2006, where he is currently a Professor. His research interests include electromagnetic field analysis, high-frequency methods, metamaterial antennas, radomes, and stealth technology.